nanotoday

REVIEW

Designing nanostructured Si anodes for high energy lithium ion batteries

Hui Wu [a], Yi Cui [a,b,∗]

[a] *Department of Materials Science and Engineering, Stanford University, Stanford, CA 94305, USA*
[b] *Stanford Institute for Materials and Energy Sciences, SLAC National Accelerator Laboratory, 2575 Sand Hill Road, Menlo Park, CA 94025, USA*

Summary   High energy lithium ion batteries are in demand for consumer electronics, electric-drive vehicles and grid-scale stationary energy storage. Si is of great interest since it has 10 times higher specific capacity than traditional carbon anodes. However, the poor cyclability due to the large volume change of Si upon insertion and extraction of lithium has been an impediment to its deployment. This review outlines three fundamental materials challenges associated with large volume change, and then shows how nanostructured materials design can successfully address these challenges. There have been three generations of nanostructure design, encompassing solid nanostructures such as nanowires, hollow nanostructures, and clamped hollow structures. The nanoscale design principles developed for Si can also be extended to other battery materials that undergo large volume changes.

Introduction

Rechargeable batteries have been critical for enabling portable consumer electronics and are beginning to be used in electric vehicles. They are also becoming an attractive option for large-scale stationary energy storage [1—6]. For mobile applications, high energy (per weight and volume) is the most important parameter since it determines the usage time per charge [4]. For stationary applications, cost is the most important design parameter, and high energy batteries could help reduce the cost per unit of stored energy [1,7,8].

Therefore, obtaining high energy density has been a major focus of recent battery research.

Compared to other technologies, lithium-ion batteries (LIBs) are the most popular rechargeable batteries due to their relatively high energy density, good cycle life, and good power performance [1—3,5,6,8,9]. LIBs are the dominant power source for portable electronics and show great promise for vehicle electrification. However, existing LIB technology is reaching its limit in energy density (per volume) and specific energy (per weight). The existing technology is based on the combination of a carbon anode and a lithium metal oxide or phosphate cathode ($LiCoO_2$, $LiMn_2O_4$, $LiFePO_4$) [6]. The relatively low capacity of the electrodes (370 mAh/g for graphite carbon and 140—170 mAh/g for lithium metal oxide/phosphate) limit the total specific energy of the cell [3].

∗ Corresponding author. Tel.: +1 650 723 4613.
   E-mail address: yicui@stanford.edu (Y. Cui).

Table 1 Comparison of various anode materials (all the capacity numbers are based on materials in the delithiated state except lithium metal).

| Materials	Li	C	$Li_4Ti_5O_{12}$	Si	Sn	Sb	Al	Mg
Density (g/cm^3)	0.53	2.25	3.5	2.3	7.3	6.7	2.7	1.3
Lithiated phase	Li	LiC_6	$Li_7Ti_5O_{12}$	$Li_{4.4}Si$	$Li_{4.4}Sn$	Li_3Sb	LiAl	Li_3Mg
Theoretical specific capacity (mAh/g)	3862	372	175	4200	994	660	993	3350
Volume change (%)	100	12	1	420	260	200	96	100
Potential versus Li (V)	0	0.05	1.6	0.4	0.6	0.9	0.3	0.1

To increase the energy content of lithium-ion batteries, significant research has been devoted to finding higher-capacity electrode materials. On the cathode side, sulfur and oxygen-based positive electrodes have recently been intensely researched [10—12]. On the anode side, alloy anodes have shown the most promise. An ideal anode material should possess high gravimetric and volumetric capacity, a low potential against cathode materials, long cycle life, light weight, environmental compatibility, low toxicity, and low cost [1,13]. Based on the specific capacity alone, pure lithium metal is clearly the best anode material since it does not carry any dead weight. However, the electroplating of dendritic lithium during charging can cause an internal short circuit, posing severe safety concerns [1]. Because of this, Si is the most attractive choice for the anode material for the reasons discussed below.

Opportunities and challenges for Si anodes

Table 1 compares the properties of different anode materials. Among them, Si has the highest gravimetric capacity (4200 mAh/g, lithiated to $Li_{4.4}Si$) and volumetric capacity (9786 mAh/cm^3 calculated based on the initial volume of silicon) among all the choices other than lithium metal; in addition, it has a relatively low discharge voltage (the average delithiation voltage of Si is 0.4 V) [14]. Si is also the second-most abundant element in the earth's crust, and it is environmentally benign. Finally, the semiconductor industry has developed a large and mature infrastructure for processing Si.

Unfortunately, Si-based electrodes typically suffer from poor capacity retention [13,15—19]. Early studies on Si anodes demonstrated rapid capacity fading during cycling. Fig. 1 shows an example of the charge/discharge curves of Si powder with an average size of 10 μm [20]. High capacity is achieved on the first lithiation, but capacity quickly fades with cycle number. After only five cycles, the reversible capacity of the Si electrode drops by 70%. In addition, the irreversible capacity loss of this Si anode during the first cycle is too high (2650 mAh/g) for practical application, as demonstrated by the Columbic efficiency of 25%. The capacity fade and large initial irreversible capacity for Si anodes are due to the large volume changes during the lithium insertion and extraction processes.

According to the equilibrium phase diagram, when lithium is inserted into Si, Si should experience a series of phase transformations, theoretically resulting in multiple voltage plateaus in the galvanostatic voltage curve (Fig. 2, black line) [14]. However, this only takes place at
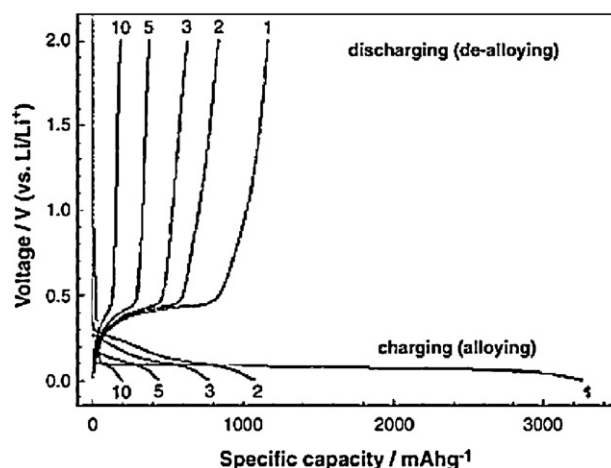
Figure 1 Galvanostatic charge—discharge profiles for a micro-Si (10 μm particle) anode [20].

high temperature. At room temperature, crystalline Si goes through a single crystalline-to-amorphous phase transformation during the first lithiation and remains amorphous afterwards (Fig. 2, green and red line).

In some instances, a metastable $Li_{15}Si_4$ phase has been identified at potentials lower than 50 mV versus lithium at room temperature [17,21,22]. When transforming from
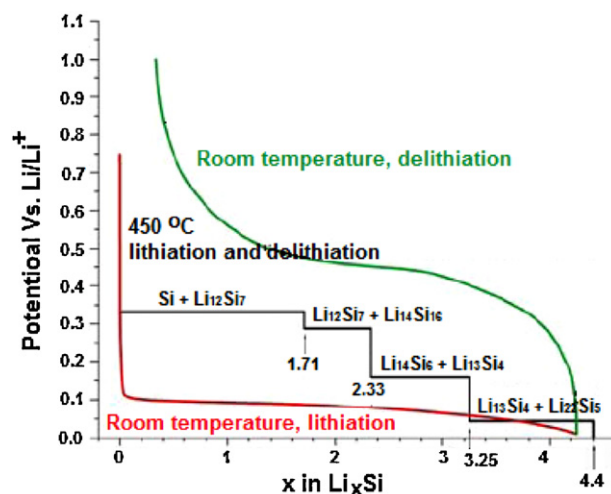

Figure 2 Si electrochemical lithiation and delithiation curve at room temperature and high temperature. Black line: theoretical voltage curve at 450 °C. Red and green line: lithiation and delithiation of crystalline Si at room temperature, respectively.

Si to $Li_{4.4}Si$, the volume expansion is about 420%. The volume expansion versus the concentration of lithium is calculated to be nearly linear [16]. Various ensemble methods [22—25], including X-ray diffraction and nuclear magnetic resonance, have been used to study the amorphization process; these studies have primarily shown experimental evidence for the crystalline-to-amorphous phase transition and have also provided information on the local atomic structure of the amorphous phase. Computational studies have provided insights such as stable atomic arrangements and diffusion energy barriers [21,24,26—29]. In addition, atomic force microscopy has been used to show that volume expansion occurs during lithiation and contraction occurs during delithiation of Si thin films [30—34]. Based on the studies of our own and others, we outline three fundamental materials challenges to using Si as a viable battery electrode, as illustrated in Fig. 3.

(1) *Material pulverization*. The large volume expansion/contraction during lithium insertion/extraction induces large stresses. These stresses can cause cracking and pulverization of the Si, which leads to loss of electrical contact and eventual capacity fading (Fig. 3a). This mechanism probably accounts for most of the capacity fade observed in early studies using bulk Si, films, and large particles of Si. For example, an AFM study of the anode surface has revealed that cracking occurs during the Li-extraction stage [35—37].

(2) *Morphology and volume change of the whole Si electrode*. The large volume changes also cause significant challenges at the level of the entire electrode. During lithiation, Si particles expand and impinge on each other. During delithiation, Si particles contract, which can result in detachment of their surrounding electrical connections. This drastic electrode morphology change can further contribute to capacity fading. In addition, the total volume of the whole Si anode also increases and decreases upon lithiation and delithiation, leading to electrode peel-off and failure, which creates challenges for full cell design.

(3) *Solid-electrolyte interphase*. When the potential of the anode is below ~1 V versus Li/Li^+, the decomposition of the organic electrolyte at the electrode surface is thermodynamically favorable. The decomposition product forms a layer on the electrode material surface called the ''solid-electrolyte interphase'' (SEI). This layer needs to be dense and stable, and it should be ionically conducting and electronically insulating in order to prevent further side chemical reactions from occurring. The formation of this passivating SEI film on the Si surface has been confirmed by HRTEM, FTIR, and XPS [38—41]. The SEI films consist mainly of Li_2CO_3, various lithium alkylcarbonates ($ROCO_2Li$), LiF, Li_2O, and nonconductive polymers [38—40]. The SEI stability at the interface between Si and the liquid electrolyte is a critical factor for obtaining long cycle life. However, the large volume change makes it very challenging to form a stable SEI. As illustrated in Fig. 3b, Si particles expand
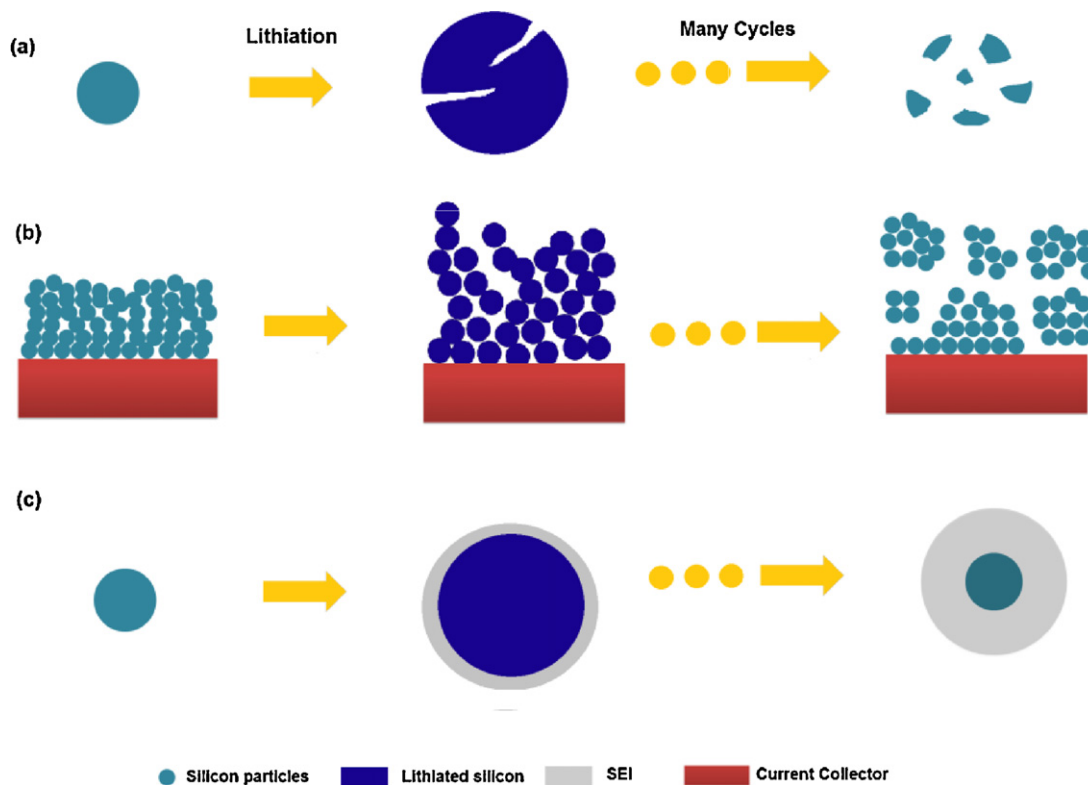
Figure 3 Si electrode failure mechanisms: (a) material pulverization. (b) Morphology and volume change of the entire Si electrode. (c) Continuous SEI growth.
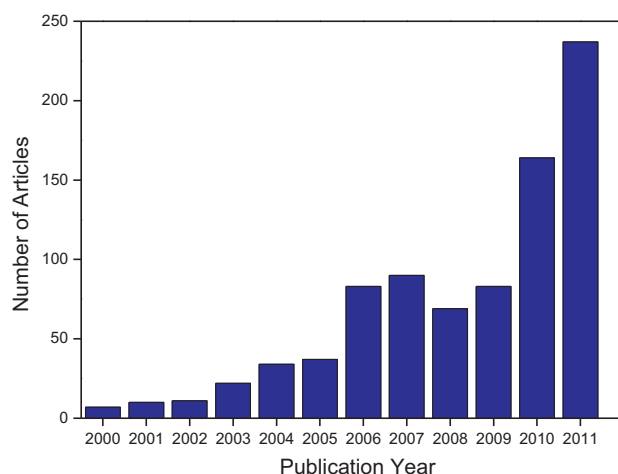
Figure 4 Charting the number of peer-reviewed publications on the use of Si materials for lithium ion battery electrodes as a function of the year published (results collected using the ISI Web of Science database with ''Si'' and ''lithium ion battery'' as search items).

out towards the electrolyte upon lithiation and contract during delithiation. The SEI formed in the lithiated (expanded) state can be broken as the particle shrinks during delithiation. This re-exposes the fresh Si surface to the electrolyte and the SEI forms again, resulting in thicker and thicker SEI upon charge/discharge cycling.

Nanostructured Si anodes

In the past decade, Si electrodes have attracted increasing research interest from the community (Fig. 4). The number of publications increased from 40 in 2005 to 240 in 2011. Various structural designs of Si materials have been proposed to overcome the three challenges mentioned above, and discernible progress has been made. Our group has conducted research into the rational design of a variety of nanostructured Si electrodes. We have gone through three generations of nanostructure design, encompassing solid, hollow, and clamped hollow nanostructures, and we have generated unique designs that successfully address these challenges.

Solid Si nanostructures

Si Nanowires (NWs)
At the end of 2007, we reported a Si anode design concept utilizing Si NWs prepared by the vapor—liquid—solid synthesis method; these electrodes exhibited significantly improved electrochemical performance compared to thick films and large particles (Fig. 5) [19]. These NWs are directly grown onto stainless steel current collectors, so one end of each NW is bonded to the metal substrate. Such Si NW electrodes have several exciting features as battery anodes:

(1) The NW array provides sufficient empty space between adjacent nanowires to accommodate the volume change associated with alloying and de-alloying of Li (schematically shown in Fig. 5a and b).

(2) Each Si NW is electrically connected to the metallic current collector, thus enabling robust electrical contact to be maintained; moreover, such an architecture allows for all nanowires to contribute to the capacity (schematically shown in Fig. 5a and b).

(3) The Si NWs feature continuous one-dimensional electronic pathways, allowing for efficient charge transport and making conductive carbon additives and polymer binders unnecessary. This is in contrast to the inefficient hopping of electrons between particles in traditional slurry-coated battery electrodes.

(4) Nanostructured Si anodes are more resistant to fracture than larger Si structures. This is because, in general, the total elastic energy stored in a small nanostructure during deformation may not be sufficient to drive crack initiation and propagation. In other words, for smaller structures, the stress-relief volume accompanying crack growth is not significant enough to overcome the surface energy penalty associated with the crack growth.

These features allow Si NW anodes to achieve significantly improved performance compared to previous studies. The Si NWs achieved nearly the theoretical charge capacity of Si and maintained a discharge capacity close to 75% of this maximum, with little fading over 10 cycles (Fig. 5c and d). The nanosize effect and superior mechanical properties of Si nanowires can be further confirmed by observing the NW morphology before and after electrochemical reactions. Pristine, unreacted Si NWs were crystalline with smooth sidewalls (Fig. 5e) and had an average diameter of 89 nm. After lithiation, the Si NWs had roughly textured sidewalls (Fig. 5f), and the average diameter increased to 141 nm. Despite the large volume change, the Si NWs remained intact and did not break into smaller particles. They also appeared to remain in contact with the current collector, suggesting minimal capacity fade due to electrically disconnected material during cycling.

Following this first demonstration of rational Si NW design, there were many other related studies [24,27,42—63]. For example, Si NWs can be prepared by a scalable supercritical fluid—liquid—solid (SFLS) method. These solution-based Si NWs can be coated with carbon, and demonstrate good performance (reversible capacities of 1500 mAh/g were observed for 30 cycles) [63]. Schulz et al. demonstrated that a Si nanofiber anode can also be synthesized by an electrospinning method. Their method involves using Si_6H_{12} as the Si precursor in a polymer carrier during electrospinning [64]. The Si nanofibers show relatively high, stable capacities. Peng et al. [44] and Flake et al. [62,65] reported Si nanowire anodes fabricated by metal-induced chemical etching of Si wafers. This method has the potential for precise control of crystal orientation and doping [47]. The Zhu group reported data from carbon-coated Si NW array films prepared by metal catalytic etching of Si and pyrolyzing of a carbon aerogel, and the capacities of the films were from the carbon-coated Si NWs exclusively, since the Si wafer substrates were completely transformed into Si NWs [43]. It is believed that the carbon coating enhances the
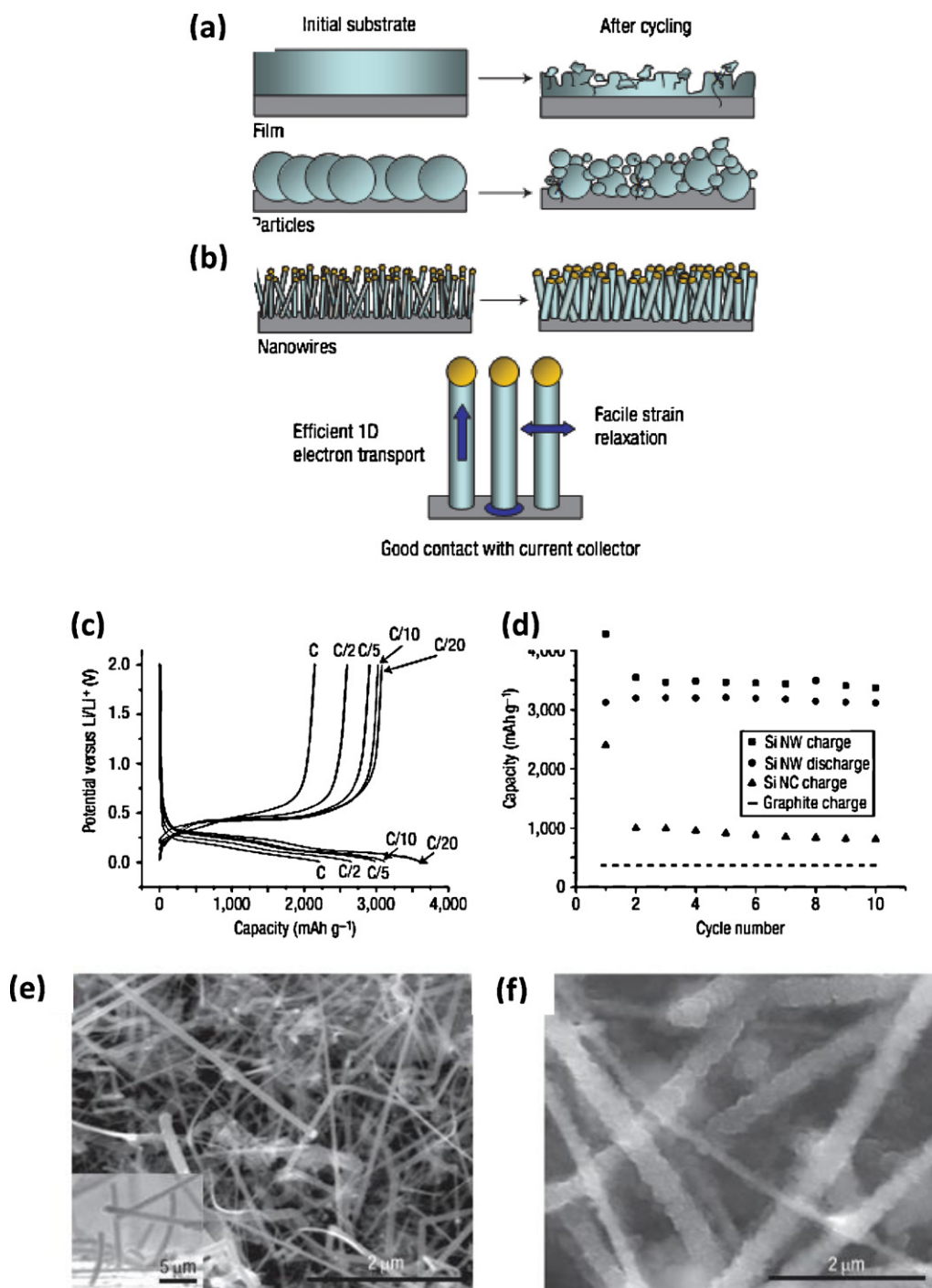
Figure 5 (a) Schematic of morphological changes that occur in Si during electrochemical cycling. The volume of Si anodes changes by about 400% during cycling. As a result, Si films and particles tend to pulverize during cycling. (b) Si NWs grown directly on the current collector do not pulverize or break into smaller particles after cycling. Rather, facile strain relaxation in the NWs allows them to increase in diameter without breaking. (c) The voltage profiles for the Si NWs cycled at different currents. (d) Capacity versus cycle number for the Si NWs at the C/20 rate. (e and f) SEM image of pristine Si NWs before (e) and after (f) electrochemical cycling [19].

electrochemical performance. Indeed, rapid capacity fading of the uncoated Si NW film electrode was observed after 10 cycles, while carbon-coated Si NW electrodes exhibited a stable reversible capacity of 1326 mAh/g after 40 cycles [43].

Core—shell Si NWs
A key materials design principle learned from the studies of Si NWs is to develop methods to maintain electrical connection without pulverization. A powerful concept is the core—shell NW, where the core material is structurally
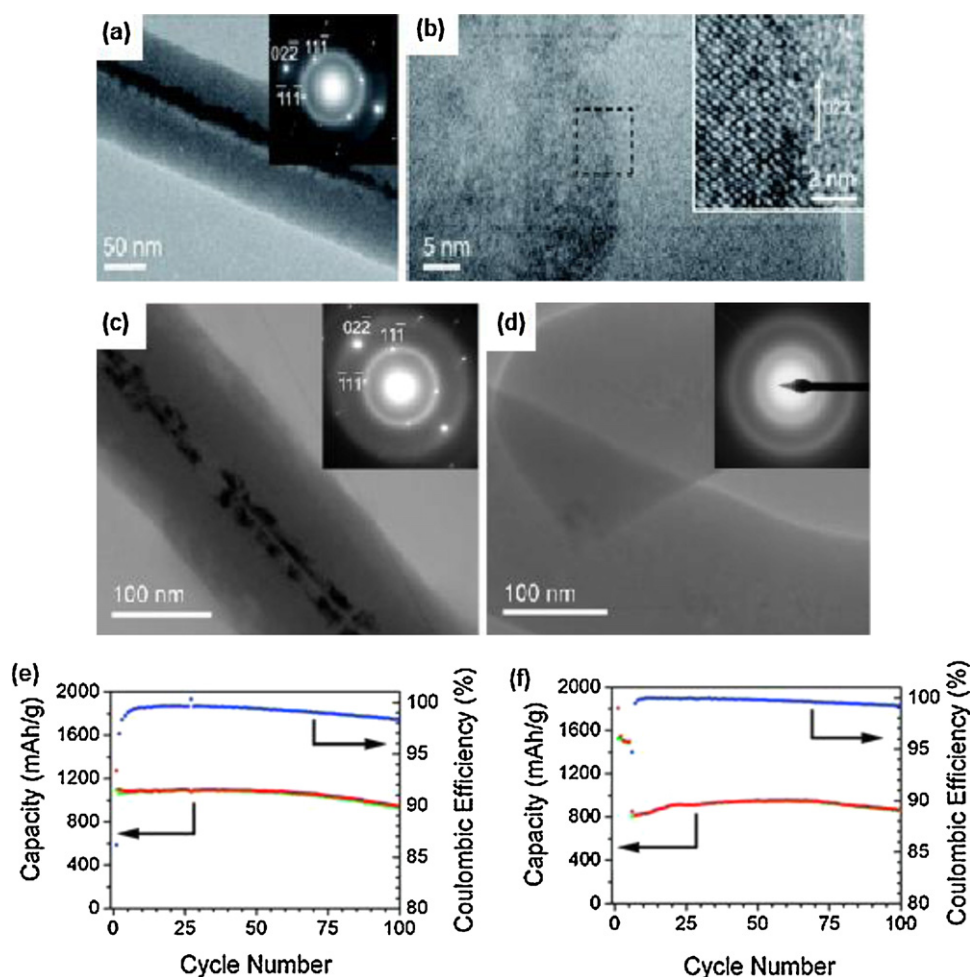
Figure 6 (a) TEM and (b) HRTEM images of NWs before cycling (grown for 40 min). (c) TEM and SAED (inset) images of a NW after 15 cycles with cutoff of 150 mV. (d) TEM and SAED (inset) images of NWs after 3 cycles with cutoff of 10 mV. (e and f) Charge (red) and discharge (green) capacity and Coulombic efficiency (blue) versus cycle number for the core—shell NWs with different low voltage cutoffs and power rates. (e) 150 mV cutoff and 0.2 C. (f) 150 mV cutoff, 0.1 C for 5 cycles then 0.8 C [39].

stable and electrically conducting and the shell material is the active Si for storing lithium ions. Our group demonstrated the first core—shell NW concept by developing crystalline-amorphous core—shell SiNWs that showed significant improvement in power rate and cycle life [39]. The a-Si reacts with lithium at a slightly higher potential than the c-Si. By controlling the charging potential to remain above the c-Si amorphization potential of 120 mV versus Li/Li$^+$, only the amorphous Si shell is lithiated, preserving the crystalline core as a mechanical support and an efficient transport pathway.

We developed a simple method to grow crystalline-amorphous core—shell Si NWs without changing the growth temperature to form the crystalline and amorphous regions. The growth was conducted directly on stainless steel (SS) current collectors in a SiH$_4$ CVD furnace. Transition metals in SS, such as Ni, Fe, or Cr, are believed to catalyze the growth by a direct vapor—solid process. Fig. 6a and b shows TEM images and SAED patterns from such a core—shell structure. To confirm that the core—shell structure is robust enough for mechanical and electrical support after cycling, we investigated the morphology and structure of NWs after cycling.
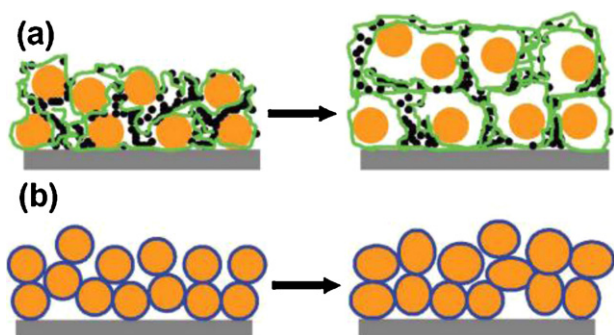
Two samples cycled with either 10 or 150 mV cutoffs are compared (Fig. 6c and d). At 150 mV, the crystalline core is maintained, while at 10 mV the NW becomes completely amorphous. Such crystalline-amorphous core—shell SiNWs were shown to have 90% capacity retention over 100 cycles with a capacity of 1000 mAh/g (Fig. 6e and f).

We have also extended the core—shell concept by synthesizing carbon—Si core—shell NWs, fabricated by CVD of amorphous Si onto carbon nanofibers (CNFs) [40]. Similarly to the crystalline Si core in the crystalline-amorphous core—shell SiNWs, carbon cores function as efficient electron transport pathways and stable mechanical supports. However, the difference is that the carbon core, due to its small capacity, has little structural or volume changes even when lithiating to 10 mV versus Li/Li$^+$. Charging to this low potential allows for much higher utilization (2000 mAh/g) of the specific charge capacity of a-Si. In addition, CNFs are commercially available in large quantities, which makes the mass production of C—Si core—shell NWs easily achievable. Other core—shell nanowire designs have also been realized by using different core materials, including metal silicides [66,67], nitride [68], and carbon nanotubes [69—80].

Si nanoparticles

Si nanoparticles with small enough diameters should also be able to undergo large volumetric strains without mechanical fracture [81–86]. Compared to NWs, the challenge for Si nanoparticles is how to electrically connect them to the current collector and how to maintain such a connection after repetitive volume changes. The traditional slurry coating method exploits conductive carbon and PVDF binder additive, which have not worked well for Si (Fig. 7a). In the past several years there has been research on developing novel methods for electrically connecting Si nanoparticles. Our group developed a method to prepare Si particle anodes where amorphous Si is deposited onto electrode structures; the amorphous Si acts as an inorganic glue to fuse all the particles together and bind them onto the current collector (Fig. 7b) [87]. This inorganic glue can help solve the issue of the loss of electrical contact in Si particle anodes prepared with conventional slurry methods. We have used this method to successfully cycle both nanoparticles and microparticles. With a limited charge capacity of 1200 mAh/g, the prepared 200 nm Si particle anode showed stable cycling up to 130 cycles in a half cell test. With a limited charge capacity of 800 mAh/g, the 8 μm Si particles can be cycled over 200 cycles in half cell tests. In another study, we used the CVD-deposited inorganic glue to physically and electrically connect Si nanoparticles to Si NWs [88]. When compared with bare Si NW anodes, the areal capacity was increased significantly without using long CVD deposition times.

Another way to improve the electrochemical cycling performance of Si nanoparticle electrodes is to explore new polymer binder materials [89,90]. Two examples are given here. Through a combination of advanced materials synthesis, spectroscopic analysis, and theoretical simulations, Liu et al. developed a new conductive binder to address the volume change problems in Si. Their integrated experimental and theoretical results show that the developed polymer features much-improved electronic conductivity

and robust mechanical binding forces, which simultaneously maintains electrical connectivity and accommodates the Si volume change. Composite electrodes based on Si particles and the PFFOMB (poly (9,9-dioctylfluorene-co-fluorenone-co-methylbenzoic acid)) binder, without any conductive additive, exhibit high capacity, long-term cycling, low overpotential between charge and discharge, and good rate performance. In another study, Yushin et al. showed that mixing Si nanoparticles with alginate, a natural polysaccharide extracted from brown algae, yields stable Si nanoparticle anodes. These applications of new high performance binders are low-cost and compatible with current slurry manufacturing, and as such are very attractive.

Hollow Si nanostructures

Compared to solid structures, hollow structures provide empty interior space for the volume expansion, which offers numerous advantages, including the development of lower diffusion-induced stresses, as demonstrated here. A finite element model was developed to calculate the diffusion-induced stress during lithiation of hollow Si nanospheres (Fig. 8). The modeling results show that the maximum
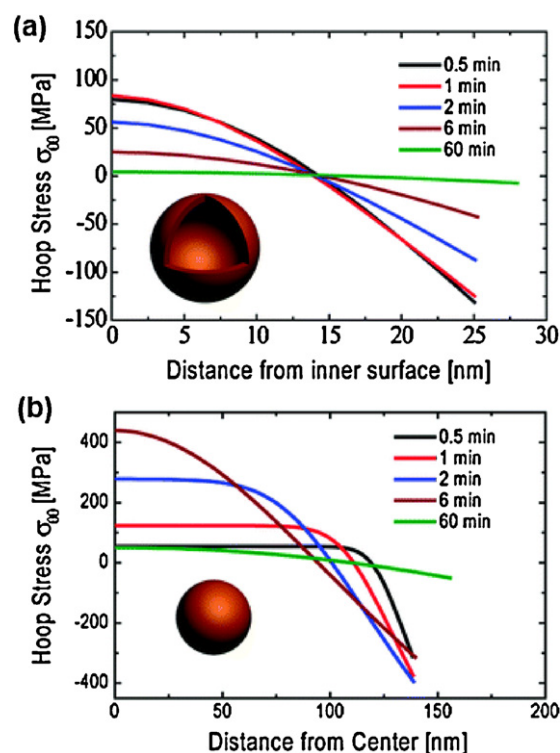

Figure 7   Schematic illustration of the morphology change of Si particle films before and after charge–discharge cycling. (a) Si particle film on SS substrate prepared with conventional slurry method, where the small black particles indicate carbon black and green lines indicate PVdF chains. After cycling, the Si particles lose electrical contact with the surrounding particles. (b) Si particles fused together and bonded onto the SS substrate by a-Si inorganic glue, where the blue rings are the a-Si coating. After cycling, the particle film still maintains an interconnected porous structure, where little loss of electrical contact occurs [87].

Figure 8   Theoretical modeling of stress evolution during lithiation in a hollow sphere versus a solid sphere with the same volume of Si. (a) Hoop stress ($\sigma_{\theta\theta}$) evolution of a hollow Si sphere at a lithiation rate of C/10 for 0.5, 1, 2, 6, and 60 min. The inset shows a schematic of the hollow Si sphere ($R_{in} = 175$ nm, $R_{out} = 200$ nm). (b) Hoop stress ($\sigma_{\theta\theta}$) evolution of a solid Si sphere at a lithiation rate of C/10 for 0.5, 1, 2, 6, and 60 min. The inset shows a schematic of the solid Si sphere ($R = 138$ nm) that has the same volume of the hollow sphere. Positive stress values indicate tensile stress, while negative values indicate compressive stress [91].
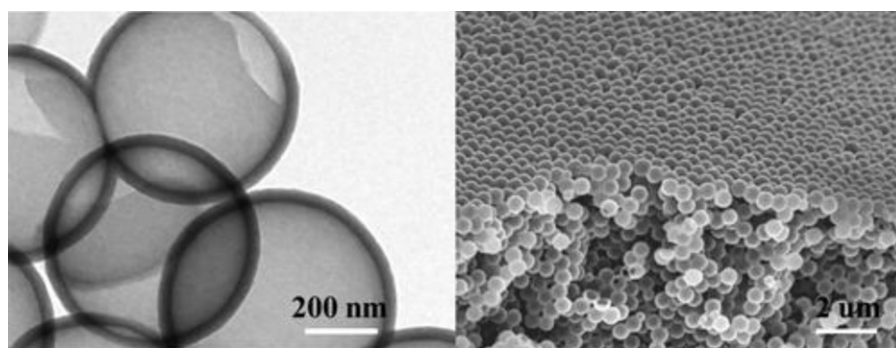
Figure 9   TEM and SEM images of Si nanospheres synthesized from silica nanoparticle templates [91].

tensile stress (that which would affect fracture) in a hollow Si sphere is five times lower than that in a solid sphere with an equal volume of Si [91]. This significant difference in the maximum tensile stress shows the unique advantage of a hollow structures; these lower stress values mean that the hollow nanostructures will fracture less readily.

Better cycling stability of hollow Si nanostructures has also been shown experimentally [91,92]. To fabricate hollow nanospheres, we employed a template approach using solid silica nanospheres. Interconnected Si nanospheres with an inner radius of ∼175 nm and an outer radius of ∼200 nm have been synthesized with this method (Fig. 9). A reversible Li discharge capacity of 2725 mAh/g has been achieved for the first cycle from this electrode. The discharge capacity degrades only 8% per 100 cycles during the 700 total cycles, showing good electrochemical stability of the nanospheres. Moreover, due to the lower stresses present, the hollow nanospheres can withstand extremely high charge/discharge rates. Even at 10 C, 57% of the 0.2 C capacity remained [91].

The electrochemical characteristics of hollow Si tubes have also been explored and have been shown to exhibit good performance [93−95]. For example, Cho's group fabricated novel Si nanotube structures by reductive decomposition of Si precursor inside anodic alumina templates [95]. The use of Si nanotubes increased the surface area accessible to the electrolyte, allowing lithium ions to intercalate from both the interior and the exterior of the nanotubes. The nanotube electrodes demonstrated reversible charge capacities of ∼3200 mAh/g with capacity retention of 89% after 200 cycles at a rate of 1 C in practical lithium ion cells with improved rate stability [95].

Hollow Si nanostructures with clamping

As stated above, the pulverization problem of Si electrodes can be successfully addressed by employing various nanostructures including solid nanowires, nanoparticles, hollow spheres and tubes. These nanostructures can effectively withstand the stress induced by heterogeneous changes in the volume of Si anodes without fracture. However, the problem of the unstable SEI remains unsolved by using these nanostructures. In addition, these materials cannot prevent volume changes at the whole electrode level since they still expand towards the outside when lithiated.

Detailed failure mechanisms of the SEI layer on Si are shown in Fig. 10a. Electrolyte decomposition occurs due to the low potential of the anode and forms an SEI layer on the electrode surface during battery operation. The SEI layer is an electronic insulator but a lithium ion conductor; ideally, this results in the SEI eventually terminating its growth at a certain thickness [96]. Even though Si nanostructures resist fracture, their interface with the electrolyte is not static due to repetitive volume expansion and contraction [16,17,22,94]. As schematically shown in Fig. 10a and b, both solid and hollow Si structures expand out towards the electrolyte upon lithiation and contract during delithiation. The SEI formed in the lithiated expanded state can be broken as the nanostructure shrinks during delithiation. This re-exposes the fresh Si surface to the electrolyte and more SEI forms, resulting in a thicker and thicker SEI film upon charge/discharge cycling. This results in battery performance degradation through (a) the consumption of
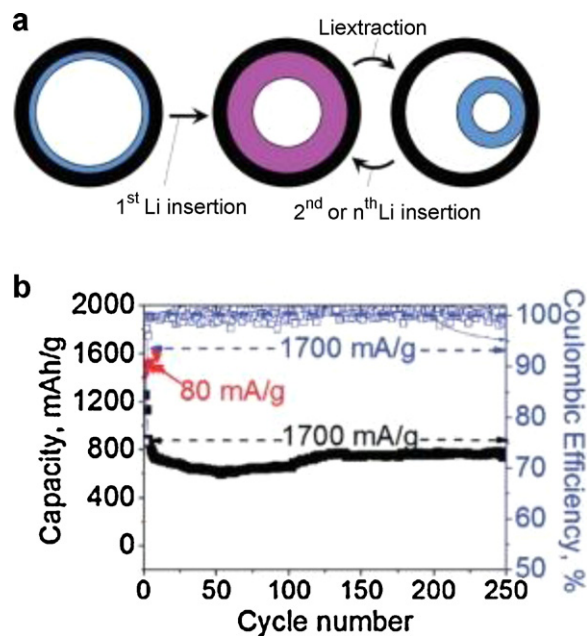
Figure 10   (a) Results of the computational modeling of shape changes of a Si tube inside a rigid nanopore during reaction with Li. (b) deintercalation capacity retention and Coulombic efficiency for the sample containing 33 wt% Si. The reported capacity is normalized by the total weight of C and Si [97].
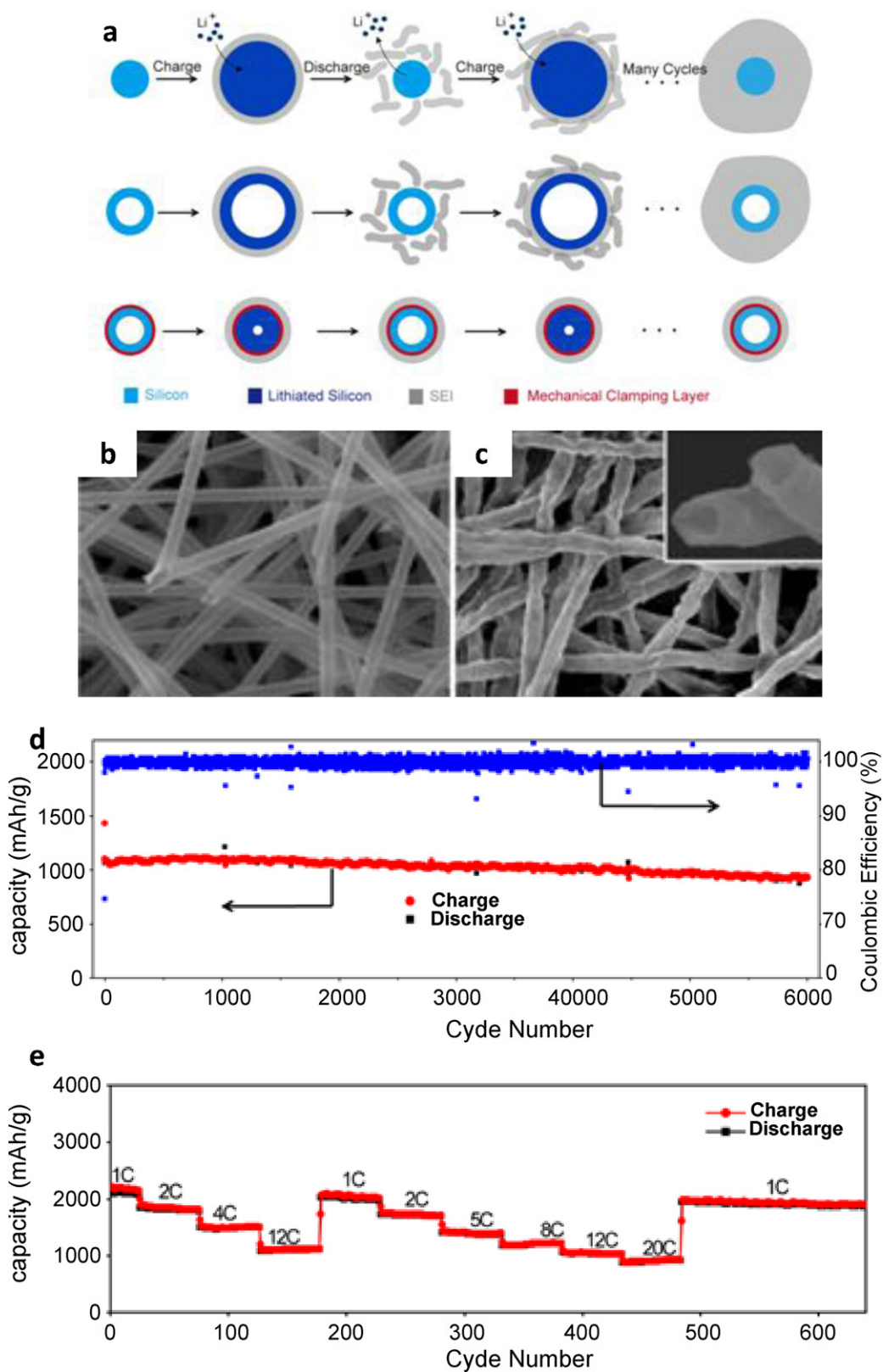
Figure 11   (a) Schematic of SEI formation on Si surfaces. Designing a mechanical constraining layer on the hollow Si nanotubes can prevent Si from expanding outside towards the electrolyte during lithiation; as a result, a thin and stable SEI can be built. (b and c) SEM images of Si nanotubes with surface clamping before and after electrochemical cycles. (d) Lithiation/delithiation capacity and Coulombic efficiency of nanotubes cycled at 12 C for 6000 cycles. There is no significant capacity fading after 6000 cycles. (e) nanotubes cycled at various rates from 1 C to 20 C [98].

electrolyte and of lithium ions during continuous SEI formation, (b) the electrically insulating nature of the SEI degrading the electrical contact between the current collector and anode material, (c) the long lithium diffusion distance through the thick SEI and (d) possible electrode material degradation caused by mechanical stress from the thick SEI. The formation of a stable SEI is critical for realizing long cycle life in Si anodes; this is also generally true for other battery electrode materials that undergo large volume changes. By engineering the microstructure and surface chemistry, nanoscale Si electrodes provide an exciting opportunity to study the SEI formation mechanisms during electrochemical reactions. Based on the in-depth understanding of SEI formation mechanisms, it is possible to overcome the unstable SEI formation problem by specialized nanostructure design of Si or Si-based composite electrodes. Yushin et al. reported a successful control of SEI growth on Si nanotubes with a rigid carbon outer shell [97]. This structure shows high electrochemical performance possibly due to the management of SEI formation (Fig. 10).

We recently proposed a surface-clamped hollow Si nanostructure, termed double walled Si nanotubes, to overcome this unstable SEI problem (Fig. 11a, bottom) [98]. By using electrospun nanofiber templates, continuous Si nanotubes with an oxide coating layer on the outer surface were fabricated (Fig. 11b). The outside SiO_x coating layer is mechanically strong and can successfully prevent the Si from expanding outward while still allowing lithium ions to pass through. In addition, the electrolyte does not wet inside the nanotubes due to the extremely high aspect ratio of the continuous nanotubes. Therefore, the outer surface of the nanotubes interfaced with the electrolyte is static, allowing for a stable SEI to be built on the outer surface, as confirmed by SEM images of nanotubes after 2000 cycles (Fig. 11c). These nanotubes also derive other advantages from the nanoscale structure, such as mechanical robustness and short Li ion diffusion lengths. In addition, inward expansion does not change the morphology and volume at the whole electrode level, which is beneficial for the design of the full battery cell. As a result, these Si nanotubes show extremely high cyclability at high rates. A long cycle life (6000 cycles with 88% capacity retention), high specific charge capacity ($\sim$2970 mAh/g at C/5, $\sim$1000 mAh/g at 12 C) and fast charging/discharging rates (up to 20 C) have been demonstrated.

Besides double-walled Si nanotubes, other nanoscale materials designs have also been explored to overcome the SEI problem [83,88,99,100]. For example, our group recently developed a novel yolk—shell design for stabilized and scalable Li-ion battery electrodes (Fig. 12). Commercially available Si nanoparticles are completely sealed inside thin, self-supporting carbon shells, with rationally designed void space in between the particles and the shells. The well-defined void space allows the Si particles to expand freely without breaking the outer carbon shell, therefore stabilizing the SEI on the shell surface. High capacity (2800 mAh/g at C/10), long cycle life (1000 cycles with 74% capacity retention), and high Coulombic efficiency (99.84%) have been realized in this yolk—shell structured Si electrode. Note that the synthesis approach is carried out without special equipment and mostly at room temperature.
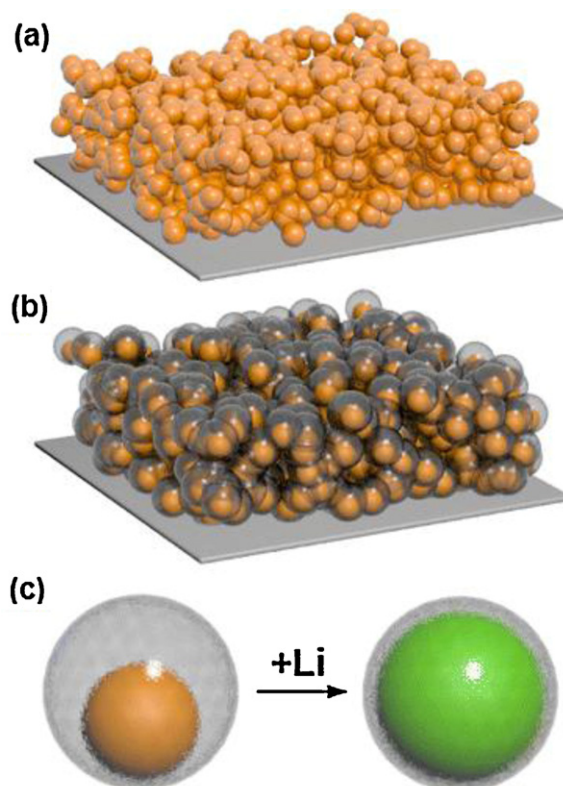
Figure 12 Schematic of the materials design for yolk—shell structures. (A) A conventional slurry-coated SiNP electrode. SEI on the surface of the SiNPs ruptures and reforms upon each SiNP during cycling, which causes the excessive growth of SEI and failure of the battery. The expansion of each SiNP also disrupts the microstructure of the electrode. (B) A novel Si@void@C electrode. The void space between each SiNP and the carbon coating layer allows the Si to expand without rupturing the coating layer, which ensures that a stable and thin SEI layer forms on the outer surface of the carbon. Also, the volume change of the SiNPs is accommodated in the void space and does not change the microstructure of the electrode. (C) A magnified schematic of an individual Si@void@C particle showing that the SiNP expands without breaking the carbon coating or disrupting the SEI layer on the outer surface [101].

Fundamental understanding of the lithiation process in nanostructures

Low dimensional Si nanostructures, especially 1D Si nanostructures with high aspect ratios, also provide an ideal model system for observation of deformation characteristics during the alloying reaction. It is of great interest to study the internal stress/strain distribution and materials failure mechanisms in nanostructured Si material systems. These studies provide the research community with a better understanding of the electrochemical alloying reaction, which further aids in the design of high performance Si anodes. Our group has studied the morphological changes in Si NWs after electrochemical cycling, and we observed interesting stepwise surface roughening and nanopore evolution (Fig. 13) [102]. Because of the small dimensions of the NWs, the pore formation can be observed clearly using
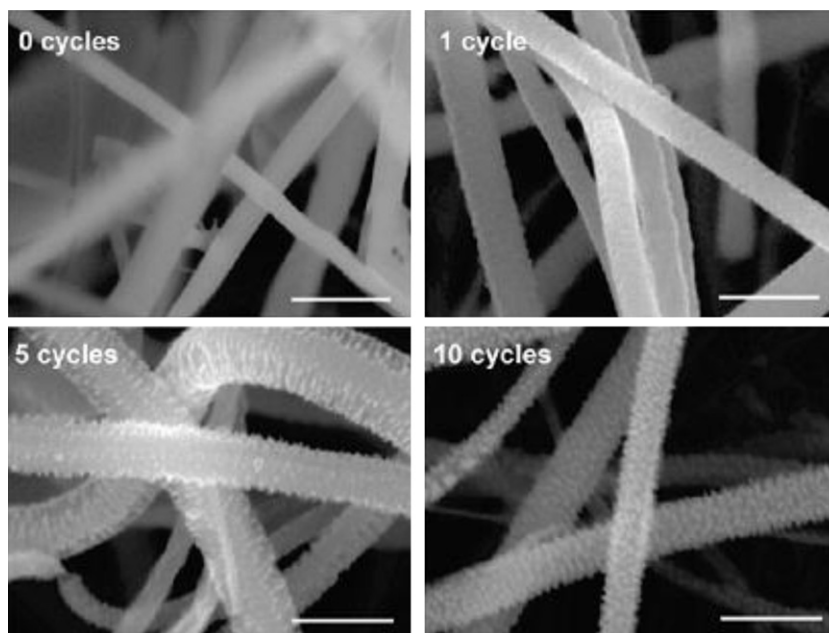
Figure 13 SEM images of SiNWs after 0, 1, 5, and 10 Li-battery cycles. All the scale bars are 200 nm [102].

electron microscopy. This study also helps explain capacity loss in Si anodes in general.

For a better understanding of electrochemical reactions inside Si nanostructures, we also studied the shape and volume changes of crystalline Si nanopillars with different orientations upon first lithiation and discovered surprising results [103]. Upon lithiation, the initially circular cross sections of nanopillars with ⟨1 0 0⟩, ⟨1 1 0⟩, and ⟨1 1 1⟩ axial orientations expanded into cross, ellipse, and hexagonal shapes, respectively (Fig. 14). This highly anisotropic expansion behavior is caused by preferred lithiation and expansion along the ⟨1 1 0⟩ direction. These results give new insight into the Si volume change process and could help in designing better battery anodes.

To study changes in the electronic conductivity during lithiation and delithiation, we developed a single NW electrochemical device that allows for the lithiation and delithiation of a single NW along with the ability to test $I-V$ characteristics and characterize structural changes at different lithiation states. We found that the electrical conductivity of individual Si NWs changes dramatically after the first lithiation and between lithiated and delithiated states.

Very recently, a nanoscale open cell electrochemical device was developed that operates inside a transmission electron microscope (TEM) [20,47,104—106], allowing real-time observation of the charging/discharging behavior of individual NW electrodes. Using this powerful tool, Liu et al. demonstrated ultrafast and full electrochemical lithiation of individual carbon-coated Si NWs by direct real-time observation using in situ transmission electron microscopy with ionic liquid electrolytes [105,106]. The Si NWs did not fracture despite the ultrahigh lithiation rates and large volume expansion. They also observed anisotropic swelling of Si NWs during lithiation. Such anisotropic expansion is consistent with our findings [103]. In other work, the effect of metallic coatings on Si expansion was studied [20].

The development of the in situ TEM technique has also resulted in deeper understanding of volume changes in Si nanoparticle electrodes. Very recently, Huang et al. developed a nanoscale open cell electrochemical device that operates inside a transmission electron microscope (TEM) [47,104—106], allowing real-time observation of the charging/discharging behavior of individual Si nanowire electrodes. Using this powerful tool, Liu et al. demonstrated ultrafast and full electrochemical lithiation of individual carbon coated Si nanowires by direct real-time observation using in situ transmission electron microscopy with ionic liquid electrolytes [105,106] (Fig. 15). The Si nanowires did not fracture despite the ultrahigh lithiation rates and ~300% volume expansion. They also observed an anisotropic swelling of Si nanowires during lithiation against either a solid electrolyte with a lithium counter-electrode or a liquid electrolyte with a LiCoO$_2$ counter-electrode (Fig. 15). Such anisotropic expansion is consistent with Cui's research [103], and is attributed to the interfacial processes of accommodating large volumetric strains at the lithiation reaction front that depend sensitively on the crystallographic orientation.

By using a similar approach, we directly observed the lithiation and expansion of yolk—shell Si nanoparticle [101]. As seen in Fig. 16, the Si particles expand in volume as Li diffuses through the carbon coating and react with the Si particles. The volume expansion is most evident in the set of particles at the bottom of the structure. In the frame labeled ''105 s'', the particles are partially lithiated, and an amorphous Li$_x$Si shell/crystalline Si core structure is readily discernible in the largest particle (the crystalline core is the region with dark contrast). After complete lithiation, the diameter of the largest Si particle increases from 185 to 300 nm and it fills the hollow space within the carbon coating. This in situ TEM tool is expected to facilitate the design of complex nanostructured Si anodes [101].
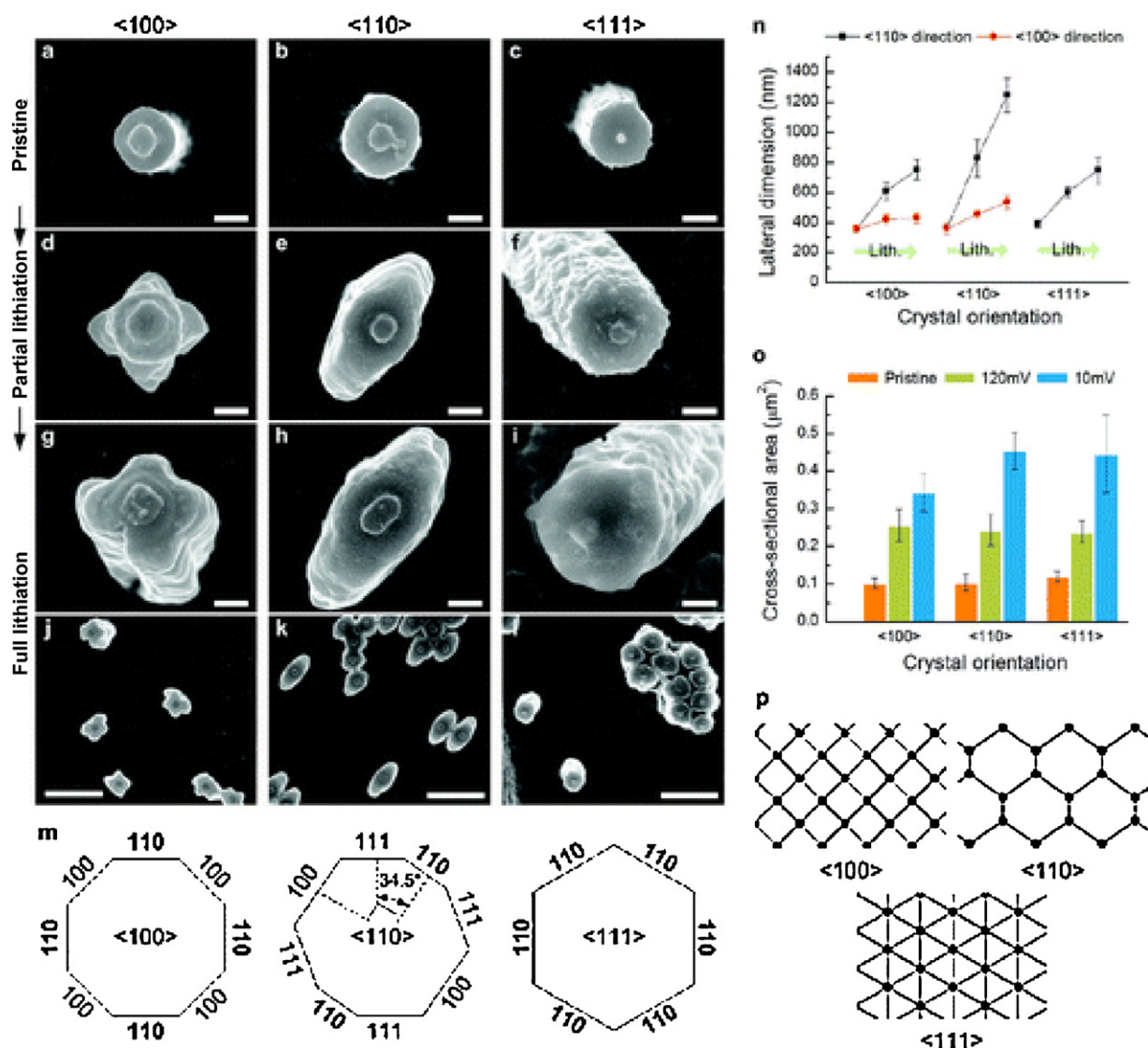
Figure 14 Anisotropic lateral expansion of crystalline Si nanopillars with three different axial orientations ($\langle 100 \rangle$, $\langle 110 \rangle$, and $\langle 111 \rangle$) upon lithiation. (a—l) Top-view SEM images of Si nanopillars of each crystal orientation and each lithiation state. The $\langle 100 \rangle$ axially oriented pillars are shown in the left column, $\langle 110 \rangle$ pillars are shown in the middle column, and $\langle 111 \rangle$ pillars are shown in the right column. The top row shows pristine pillars, the second row shows partially lithiated pillars held at 120 mV versus Li/Li$^+$, and the third row shows fully lithiated pillars held at 10 mV versus Li/Li$^+$. The images in the fourth row show low-magnification views of fully lithiated pillars of each axial orientation. Scale bars from (a—i) are 200 nm and from (j—l) are 2 μm. (m) Schematic diagram of the crystallographic orientation of the facets on the sidewalls of each of the pillars. Lithiated Si primarily expands along the 110 direction perpendicular to the nanopillar axis. (n) Statistical data of the changes in cross-sectional dimensions for the three types of nanopillars. Data is presented for pristine, partially lithiated, and fully lithiated pillars for cross-sectional expansion in both the $\langle 110 \rangle$ and $\langle 100 \rangle$ directions. (o) Statistical data of the changes in cross-sectional area for the three types of nanopillars. (p) View along three different directions of the diamond cubic lattice: $\langle 100 \rangle$, $\langle 110 \rangle$, and $\langle 111 \rangle$. It is evident that the different crystalline planes have different atomic structures [103].

Summary and outlook

In summary, Si is an attractive anode material due to its high capacity, although the large volume changes during lithiation/delithiation have been the main impediment to implementation. We have outlined three fundamental materials challenges: material pulverization at the individual Si particle level, unstable solid-electrolyte interphase, and morphology and volume change at the whole electrode level. In this review, we have presented the series of nanostructure designs that have addressed these issues. The design has gone through three generations, including solid, hollow, and clamped hollow structures. The clamped hollow structures, such as double-walled nanotubes and yolk—shell nanoparticles can address all three challenges and are the most successful designs. The nanoscale design principles developed here for Si can also be extended to other battery materials with large volume change,
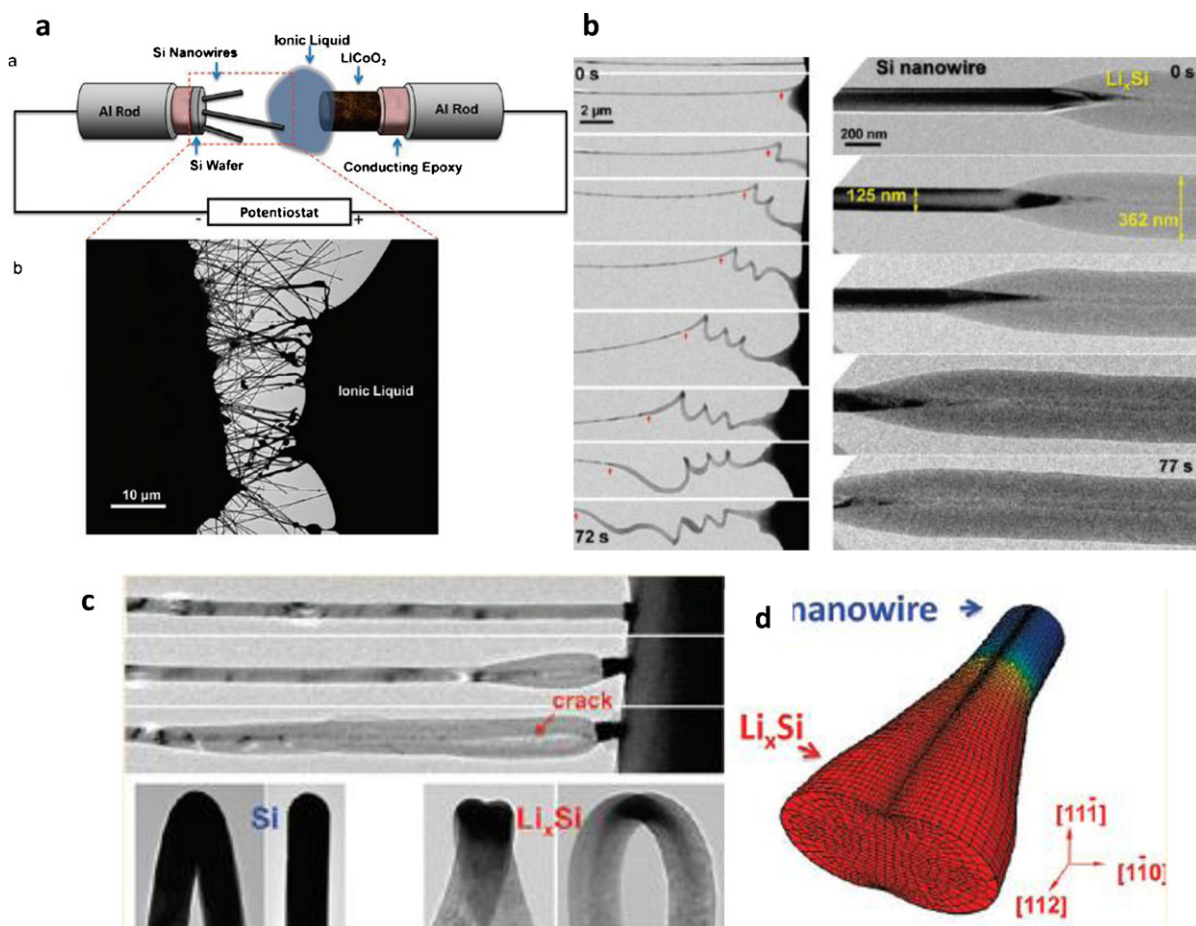
Figure 15 (a) Schematic illustration of the electrochemical device. (b) Ultrafast charging of carbon-coated and phosphorus-doped silicon nanowires. TEM images of Si nanowire after lithiation for different times are shown. (c) In situ TEM observation of anisotropic swelling of Si nanowires during lithiation. (d) 3D simulation of a progressively lithiated nanowire (i.e., the Li flux is prescribed at the front end), showing the development of the dumbbell-shaped cross section along the longitudinal direction [105].
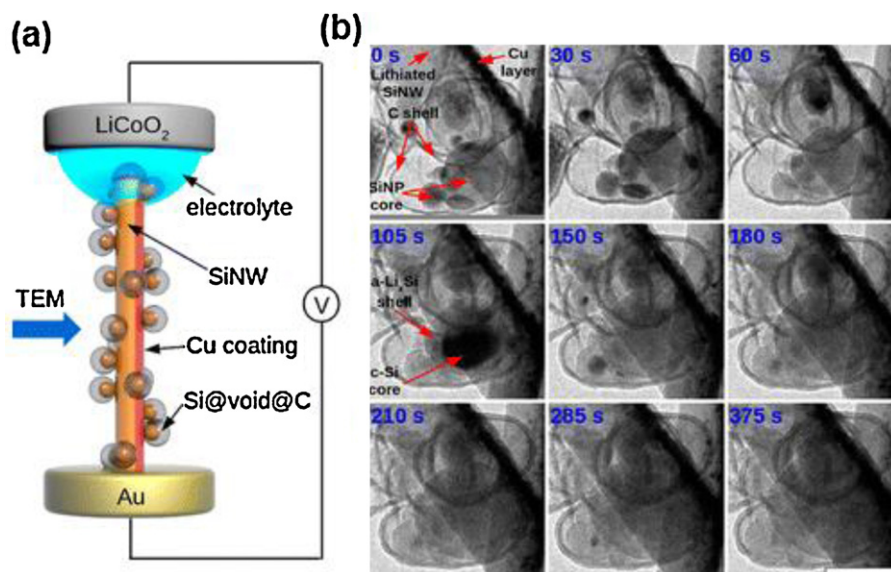
Figure 16 In situ TEM characterization of Si@void@C expansion during electrochemical lithiation. (a) Schematic of the in situ TEM device. (b) In situ TEM image. In this series of images, the Si particles are observed to expand within the outer carbon shell. Scale bar: 200 nm [101].

such as other alloy anodes and conversion material cathodes.

While nanostructured Si anodes have demonstrated great success, future research is necessary in the following areas. First, nanoscale design at the qualitative level has been established, but quantitative understanding is still needed. For example, the size-dependence of the nanostructure properties needs to be defined quantitatively. Second, the nature of the solid electrolyte interphase on Si needs to be studied, which will lead to improvements in the Coulombic efficiency. In addition, nanoscale coatings on Si are highly desirable. Third, the atomistic processes that occur during lithium insertion and extraction are still not completely understood. The use of ex situ or in situ characterization techniques, guided by multi-scale modeling and simulations, is vital to unraveling these detailed microscopic processes. Fourth, methods of packing nanostructured Si into the electrode structure and understanding deformation mechanisms at the whole electrode level are necessary. Finally, the development of large-scale, low-cost fabrication strategies for nanomaterials with desirable performance is an important challenge.

Acknowledgments

References

[1] J.M. Tarascon, M. Armand, Nature 414 (2001) 359—367.
[2] M.S. Whittingham, Chem. Rev. 104 (2004) 4271—4301.
[3] M. Armand, J.M. Tarascon, Nature 451 (2008) 652—657.
[4] D. Linden, T. Reddy, Handbook of Batteries, McGraw-Hill, New York, 2002.
[5] J. Goodenough, H. Abruna, M. Buchanan, US Department of Energy, Washington, DC, 2007.
[6] C. Liu, F. Li, L.P. Ma, H.M. Cheng, Adv. Mater. 22 (2010) E28.
[7] Y.J. Lee, H. Yi, W.J. Kim, K. Kang, D.S. Yun, M.S. Strano, G. Ceder, A.M. Belcher, Science 324 (2009) 1051—1055.
[8] B. Scrosati, J. Garche, J. Power Sources 195 (2010) 2419—2430.
[9] Y. Yang, S. Jeong, L.B. Hu, H. Wu, S.W. Lee, Y. Cui, Proc. Natl. Acad. Sci. USA 108 (2011) 13013—13018.
[10] Y. Yang, M.T. McDowell, A. Jackson, J.J. Cha, S.S. Hong, Y. Cui, Nano Lett. 10 (2010) 1486—1491.
[11] B.L. Ellis, K.T. Lee, L.F. Nazar, Chem. Mater. 22 (2010) 691—714.
[12] X.L. Ji, K.T. Lee, L.F. Nazar, Nat. Mater. 8 (2009) 500—506.
[13] J.R. Szczech, S. Jin, Energy Environ. Sci. 4 (2011) 56—72.
[14] R.A. Huggins, J. Power Sources 81 (1999) 13—19.
[15] J.O. Besenhard, J. Yang, M. Winter, J. Power Sources 68 (1997) 87—90.
[16] L.Y. Beaulieu, K.W. Eberman, R.L. Turner, L.J. Krause, J.R. Dahn, Electrochem. Solid State Lett. 4 (2001) A137—A140.

[17] L.Y. Beaulieu, T.D. Hatchard, A. Bonakdarpour, M.D. Fleischauer, J.R. Dahn, J. Electrochem. Soc. 150 (2003) A1457—A1464.
[18] X.W. Zhang, P.K. Patil, C.S. Wang, A.J. Appleby, F.E. Little, D.L. Cocke, J. Power Sources 125 (2004) 206—213.
[19] C.K. Chan, H.L. Peng, G. Liu, K. McIlwrath, X.F. Zhang, R.A. Huggins, Y. Cui, Nat. Nanotechnol. 3 (2008) 31—35.
[20] M.T. McDowell, S.W. Lee, C. Wang, Y. Cui, Nano Energy 1 (2012) 401—410.
[21] V.L. Chevrier, J.W. Zwanziger, J.R. Dahn, J. Alloys Compd. 496 (2010) 25—36.
[22] T.D. Hatchard, J.R. Dahn, J. Electrochem. Soc. 151 (2004) A838—A842.
[23] M.T. McDowell, Y. Cui, Adv. Energy Mater. 1 (2011) 894—900.
[24] I. Ryu, J.W. Choi, Y. Cui, W.D. Nix, J. Mech. Phys. Solids 59 (2011) 1717—1730.
[25] S.W. Lee, M.T. McDowell, L.A. Berla, W.D. Nix, Y. Cui, Proc. Natl. Acad. Sci. USA 109 (2012) 4080—4085.
[26] W.H. Wan, Q.F. Zhang, Y. Cui, E.G. Wang, J. Phys.: Condens. Matter 22 (2010) 415501.
[27] Q.F. Zhang, W.X. Zhang, W.H. Wan, Y. Cui, E.G. Wang, Nano Lett. 10 (2010) 3243—3249.
[28] Q.F. Zhang, Y. Cui, E.G. Wang, J. Phys. Chem. C 115 (2011) 9376—9381.
[29] S. Golmon, K. Maute, S.H. Lee, M.L. Dunn, Appl. Phys. Lett. 97 (2010).
[30] U. Maver, A. Znidarsic, M. Gaberscek, J. Mater. Chem. 21 (2011) 4071—4075.
[31] S.K. Soni, B.W. Sheldon, X.C. Xiao, M.W. Verbrugge, D. Ahn, H. Haftbaradaran, H.J. Gao, J. Electrochem. Soc. 159 (2012) A38—A43.
[32] K.L. Lee, J.Y. Jung, S.W. Lee, H.S. Moon, J.W. Park, J. Power Sources 129 (2004) 270—274.
[33] M.S. Park, G.X. Wang, H.K. Liu, S.X. Dou, Electrochim. Acta 51 (2006) 5246—5249.
[34] P.R. Raimann, N.S. Hochgatterer, C. Korepp, K.C. Moller, M. Winter, H. Schrottner, F. Hofer, J.O. Besenhard, Ionics 12 (2006) 253—255.
[35] C.M. Park, J.H. Kim, H. Kim, H.J. Sohn, Chem. Soc. Rev. 39 (2010) 3115—3141.
[36] G.K. Simon, T. Goswami, Metall. Mater. Trans. A: Phys. Metall. Mater. Sci. 42A (2011) 231—238.
[37] W.J. Zhang, J. Power Sources 196 (2011) 13—24.
[38] P. Verma, P. Maire, P. Novak, Electrochim. Acta 55 (2010) 6332—6341.
[39] R. Ruffo, S.S. Hong, C.K. Chan, R.A. Huggins, Y. Cui, J. Phys. Chem. C 113 (2009) 11390—11398.
[40] C.K. Chan, R. Ruffo, S.S. Hong, Y. Cui, J. Power Sources 189 (2009) 1132—1140.
[41] X.D. Wu, Z.X. Wang, L.Q. Chen, X.J. Huang, Electrochem. Commun. 5 (2003) 935—939.
[42] X.L. Chen, K. Gerasopoulos, J.C. Guo, A. Brown, C.S. Wang, R. Ghodssi, J.N. Culver, Adv. Funct. Mater. 21 (2011) 380—387.
[43] R. Huang, X. Fan, W.C. Shen, J. Zhu, Appl. Phys. Lett. 95 (2009).
[44] K.Q. Peng, J.S. Jie, W.J. Zhang, S.T. Lee, Appl. Phys. Lett. 93 (2008).
[45] B.M. Bang, H. Kim, J.P. Lee, J. Cho, S. Park, Energy Environ. Sci. 4 (2011) 3395—3399.
[46] H. Foll, J. Carstensen, E. Ossei-Wusu, A. Cojocaru, E. Quiroga-Gonzalez, G. Neumann, J. Electrochem. Soc. 158 (2011) A580—A584.
[47] J.Y. Huang, L. Zhong, C.M. Wang, J.P. Sullivan, W. Xu, L.Q. Zhang, S.X. Mao, N.S. Hudak, X.H. Liu, A. Subramanian, H.Y. Fan, L.A. Qi, A. Kushima, J. Li, Science 330 (2010) 1515—1520.
[48] H. Foll, H. Hartz, E. Ossei-Wusu, J. Carstensen, O. Riemenschneider, Phys. Status Solidi: Rapid Res. Lett. 4 (2010) 4—6.

[49] V. Chakrapani, F. Rusli, M.A. Filler, P.A. Kohl, J. Power Sources 205 (2012) 433–438.

[50] J.H. Cho, X.L. Li, S.T. Picraux, J. Power Sources 205 (2012) 467–473.

[51] N. Du, H. Zhang, X. Fan, J.X. Yu, D.R. Yang, J. Alloys Compd. 526 (2012) 53–58.

[52] V. Etacheri, U. Geiger, Y. Gofer, G.A. Roberts, I.C. Stefan, R. Fasching, D. Aurbach, Langmuir 28 (2012) 6175–6184.

[53] K. Karki, E. Epstein, J.H. Cho, Z. Jia, T. Li, S.T. Picraux, C.S. Wang, J. Cumings, Nano Lett. 12 (2012) 1392–1397.

[54] H. Yang, S. Huang, X. Huang, F.F. Fan, W.T. Liang, X.H. Liu, L.Q. Chen, J.Y. Huang, J. Li, T. Zhu, S.L. Zhang, Nano Lett. 12 (2012) 1953–1958.

[55] A.M. Chockla, J.T. Harris, V.A. Akhavan, T.D. Bogart, V.C. Holmberg, C. Steinhagen, C.B. Mullins, K.J. Stevenson, B.A. Korgel, J. Am. Chem. Soc. 133 (2011) 20914–20921.

[56] N.S. Hieu, J.C. Lim, J.K. Lee, Microelectron. Eng. 89 (2012) 138–140.

[57] E.L. Memarzadeh, W.P. Kalisvaart, A. Kohandehghan, B. Zahiri, C.M.B. Holt, D. Mitlin, J. Mater. Chem. 22 (2012) 6655–6668.

[58] J. Qu, H.Q. Li, J.J. Henry, S.K. Martha, N.J. Dudney, H.B. Xu, M.F. Chi, M.J. Lance, S.M. Mahurin, T.M. Besmann, S. Dai, J. Power Sources 198 (2012) 312–317.

[59] H.T. Chen, J. Xu, P.C. Chen, X. Fang, J. Qiu, Y. Fu, C.W. Zhou, ACS Nano 5 (2011) 8383–8390.

[60] X.H. Liu, J.Y. Huang, Energy Environ. Sci. 4 (2011) 3844–3860.

[61] H.T. Nguyen, F. Yao, M.R. Zamfir, C. Biswas, K.P. So, Y.H. Lee, S.M. Kim, S.N. Cha, J.M. Kim, D. Pribat, Adv. Energy Mater. 1 (2011) 1154–1161.

[62] W.L. Xu, S.S.S. Vegunta, J.C. Flake, J. Power Sources 196 (2011) 8583–8589.

[63] C.K. Chan, R.N. Patel, M.J. O'Connell, B.A. Korgel, Y. Cui, ACS Nano 4 (2010) 1443–1450.

[64] D.L. Schulz, J. Hoey, J. Smith, A. Elangovan, X. Wu, I. Akhatov, S. Payne, J. Moore, P. Boudjouk, L. Pederson, J. Xiao, J.G. Zhang, Electrochem. Solid State Lett. 13 (2010) A143–A145.

[65] W.L. Xu, J.C. Flake, J. Electrochem. Soc. 157 (2010) A41–A45.

[66] J. Xie, X.G. Yang, S. Zhou, D.W. Wang, ACS Nano 5 (2011) 9225–9231.

[67] S. Zhou, X.H. Liu, D.W. Wang, Nano Lett. 10 (2010) 860–863.

[68] Y. Yao, K.F. Huo, L.B. Hu, N.A. Liu, J.J. Ha, M.T. McDowell, P.K. Chu, Y. Cui, ACS Nano 5 (2011) 8346–8351.

[69] K. Evanoff, J. Khan, A.A. Balandin, A. Magasinski, W.J. Ready, T.F. Fuller, G. Yushin, Adv. Mater. 24 (2012) 533.

[70] H.W. Liao, K. Karki, Y. Zhang, J. Cumings, Y.H. Wang, Adv. Mater. 23 (2011) 4318–4322.

[71] G.K. Simon, B. Maruyama, M.F. Durstock, D.J. Burton, T. Goswami, J. Power Sources 196 (2011) 10254–10257.

[72] J.Y. Eom, H.S. Kwon, ACS Appl. Mater. Interfaces 3 (2011) 1015–1021.

[73] C. Martin, O. Crosnier, R. Retoux, D. Belanger, D.M. Schleich, T. Brousse, Adv. Funct. Mater. 21 (2011) 3524–3530.

[74] J.C. Guo, A. Sun, X.L. Chen, C.S. Wang, A. Manivannan, Electrochim. Acta 56 (2011) 3981–3987.

[75] L.F. Cui, L.B. Hu, J.W. Choi, Y. Cui, ACS Nano 4 (2010) 3671–3678.

[76] W. Wang, P.N. Kumta, ACS Nano 4 (2010) 2233–2241.

[77] D. Xia, Q.Z. Xue, J. Xie, H.J. Chen, C. Lv, Comput. Mater. Sci. 49 (2010) 588–592.

[78] J.Z. Wang, C. Zhong, S.L. Chou, H.K. Liu, Electrochem. Commun. 12 (2010) 1467–1470.

[79] S.L. Chou, Y. Zhao, J.Z. Wang, Z.X. Chen, H.K. Liu, S.X. Dou, J. Phys. Chem. C 114 (2010) 15862–15867.

[80] Z.B. Zhou, Y.H. Xu, W.G. Liu, L.B. Niu, J. Alloys Compd. 493 (2010) 636–639.

[81] T.H. Hwang, Y.M. Lee, B.S. Kong, J.S. Seo, J.W. Choi, Nano Lett. 12 (2012) 802–807.

[82] H.M. Jeong, S.Y. Lee, W.H. Shin, J.H. Kwon, A. Shakoor, T.H. Hwang, S.Y. Kim, B.S. Kong, J.S. Seo, Y.M. Lee, J.K. Kang, J.W. Choi, RSC Adv. 2 (2012) 4311–4317.

[83] M.T. McDowell, S.W. Lee, I. Ryu, H. Wu, W.D. Nix, J.W. Choi, Y. Cui, Nano Lett. 11 (2011) 4018–4025.

[84] X.S. Zhou, Y.X. Yin, A.M. Cao, L.J. Wan, Y.G. Guo, ACS Appl. Mater. Interfaces 4 (2012) 2824–2828.

[85] S. Iwamura, H. Nishihara, T. Kyotani, J. Phys. Chem. C 116 (2012) 6004–6011.

[86] B.S. Lee, S.B. Son, K.M. Park, J.H. Seo, S.H. Lee, I.S. Choi, K.H. Oh, W.R. Yu, J. Power Sources 206 (2012) 267–273.

[87] L.F. Cui, L.B. Hu, H. Wu, J.W. Choi, Y. Cui, J. Electrochem. Soc. 158 (2011) A592–A596.

[88] L.B. Hu, H. Wu, S.S. Hong, L.F. Cui, J.R. McDonough, S. Bohy, Y. Cui, Chem. Commun. 47 (2011) 367–369.

[89] I. Kovalenko, B. Zdyrko, A. Magasinski, B. Hertzberg, Z. Milicev, R. Burtovyy, I. Luzinov, G. Yushin, Science 333 (2011) 75–79.

[90] G. Liu, S.D. Xun, N. Vukmirovic, X.Y. Song, P. Olalde-Velasco, H.H. Zheng, V.S. Battaglia, L.W. Wang, W.L. Yang, Adv. Mater. 23 (2011) 4679.

[91] Y. Yao, M.T. McDowell, I. Ryu, H. Wu, N.A. Liu, L.B. Hu, W.D. Nix, Y. Cui, Nano Lett. 11 (2011) 2949–2954.

[92] H. Ma, F.Y. Cheng, J. Chen, J.Z. Zhao, C.S. Li, Z.L. Tao, J. Liang, Adv. Mater. 19 (2007) 4067.

[93] T. Song, H.Y. Cheng, H. Choi, J.H. Lee, H. Han, D.H. Lee, D.S. Yoo, M.S. Kwon, J.M. Choi, S.G. Doo, H. Chang, J.L. Xiao, Y.G. Huang, W.I. Park, Y.C. Chung, H. Kim, J.A. Rogers, U. Paik, ACS Nano 6 (2012) 303–309.

[94] T. Song, J.L. Xia, J.H. Lee, D.H. Lee, M.S. Kwon, J.M. Choi, J. Wu, S.K. Doo, H. Chang, W. Il Park, D.S. Zang, H. Kim, Y.G. Huang, K.C. Hwang, J.A. Rogers, U. Paik, Nano Lett. 10 (2010) 1710–1716.

[95] M.H. Park, M.G. Kim, J. Joo, K. Kim, J. Kim, S. Ahn, Y. Cui, J. Cho, Nano Lett. 9 (2009) 3844–3847.

[96] D. Aurbach, J. Power Sources 89 (2000) 206–218.

[97] B. Hertzberg, A. Alexeev, G. Yushin, J. Am. Chem. Soc. 132 (2010) 8548.

[98] H. Wu, G. Chan, J.W. Choi, I. Ryu, Y. Yao, M.T. McDowell, S.W. Lee, A. Jackson, Y. Yang, L.B. Hu, Y. Cui, Nat. Nanotechnol. 7 (2012) 309–314.

[99] H. Wu, G.Y. Zheng, N.A. Liu, T.J. Carney, Y. Yang, Y. Cui, Nano Lett. 12 (2012) 904–909.

[100] L.B. Hu, H. Wu, Y.F. Gao, A.Y. Cao, H.B. Li, J. McDough, X. Xie, M. Zhou, Y. Cui, Adv. Energy Mater. 1 (2011) 523–527.

[101] N. Liu, H. Wu, M.T. McDowell, Y. Yao, C. Wang, Y. Cui, Nano Lett. 12 (2012) 3315–3321.

[102] J.W. Choi, J. McDonough, S. Jeong, J.S. Yoo, C.K. Chan, Y. Cui, Nano Lett. 10 (2010) 1409–1413.

[103] S.W. Lee, M.T. McDowell, J.W. Choi, Y. Cui, Nano Lett. 11 (2011) 3034–3039.

[104] Y.M. Sun, X.L. Hu, W.X. Zhang, L.X. Yuan, Y.H. Huang, J. Nanopart. Res. 13 (2011) 3139–3148.

[105] X.H. Liu, H. Zheng, L. Zhong, S. Huan, K. Karki, L.Q. Zhang, Y. Liu, A. Kushima, W.T. Liang, J.W. Wang, J.H. Cho, E. Epstein, S.A. Dayeh, S.T. Picraux, T. Zhu, J. Li, J.P. Sullivan, J. Cumings, C.S. Wang, S.X. Mao, Z.Z. Ye, S.L. Zhang, J.Y. Huang, Nano Lett. 11 (2011) 3312–3318.

[106] X.H. Liu, L.Q. Zhang, L. Zhong, Y. Liu, H. Zheng, J.W. Wang, J.H. Cho, S.A. Dayeh, S.T. Picraux, J.P. Sullivan, S.X. Mao, Z.Z. Ye, J.Y. Huang, Nano Lett. 11 (2011) 2251–2258.
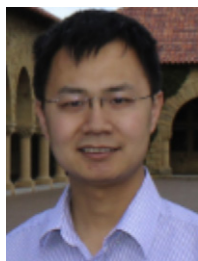
Hui Wu has been apostdoctoral research fellow in Professor Yi Cui's group since 2009. He received his BS degree in polymer science in 2004 from Tsinghua University, Beijing, China. Wu earned his Ph.D degree in materials science in 2009 from Tsinghua University under the supervision of Professor Wei Pan, with a focus on the chemical synthesis and physical properties of functional polymer and ceramic nanofibers. His research interests include applications of nanomaterials for energy storage, photovotalics, optoelectronics and flexible electronics.

Yi Cui received BS in Chemistry from University of Science and Technology of China in 1998, Ph.D in Chemistry from Harvard University in 2002. After that, he worked as a Miller Postdoctoral Fellow at the University of California, Berkeley. In 2005 he became an Assistant Professor in Department of Materials Science and Engineering at Stanford University. In 2010 he was promoted to an Associate Professor with tenure and named as David Filo and Jerry Yang Faculty Scholar.

His current research is on nanomaterials for energy storage, photovotalics, topological insulators, nanobiology and environment. He has received the Wilson Prize (2011), the David Filo and Jerry Yang Faculty Scholar (2010), the Sloan Research Fellowship (2010), the Global Climate and Energy Project Distinguished Lecturer (2009), KAUST Investigator Award (2008), ONR Young Investigator Award (2008), MDV Innovators Award (2007), Terman Fellowship (2005), the Technology Review World Top Young Innovator Award (2004), Miller Research Fellowship (2003), Distinguished Graduate Student Award in Nanotechnology (Foresight Institute, 2002), Gold Medal of Graduate Student Award (Material Research Society, 2001).